Chemical Engineering Journal 466 (2023) 143254

Contents lists available at ScienceDirect

Chemical Engineering Journal

journal homepage: www.elsevier.com/locate/cej

Photoactive nano-confined Pt in titania nanotubes (Pt-TiNT) via microwave-assisted flow synthesis

Yingjian Luo [a], Ana Serrano-Lotina [b], Felicia Febriana Budihardjo [c], Shabnam Taghipour [c,d], Shammi Akter Ferdousi [c], Liping Li [a], Juan Jose Delgado [e], Ángel López-Buendía [f], Raquel Portela [b], Wei Han [a,g], Miguel A. Bañares [b,**], King Lun Yeung [a,c,g,*]

[a] Division of Environment and Sustainability, The Hong Kong University of Science and Technology, Clear Water Bay, Kowloon, Hong Kong Special Administrative Region
[b] CSIC-ICP, Instituto de Catálisis y Petroleoquímica, Spectroscopy and Industrial Catalysis (SpeiCat), Marie Curie 2, E-28049-Madrid, Spain
[c] Department of Chemical and Biological Engineering, The Hong Kong University of Science and Technology, Clear Water Bay, Kowloon, Hong Kong Special Administrative Region
[d] Department of Civil Engineering, Sharif University of Technology, Tehran, Iran
[e] Department of Materials Sciences and Metallurgical Engineering and Inorganic Chemistry Universidad de Cadiz, Campus Universitario de Puerto Real 11519 Puerto Real, Cádiz, Spain
[f] CEINNMAT, SL, Catedratico Agustin Escardino 9, E-46980-Paterna, Valencia, Spain
[g] HKUST Shenzhen-Hong Kong Collaborative Innovation Research Institute, Futian, Shenzhen, Guangdong, China

ARTICLE INFO

Keywords:
PtO nanoparticles
Titania photocatalysts
Flow synthesis
Single-mode MW
Photocatalytic oxidation
Diclofenac
Pharmaceutical pollutants

ABSTRACT

Pt-TiNT with PtO nanoparticles dispersed within the lumen and interlayer spaces of titania nanotubes (TiNT) were prepared by a new process involving titanate nanosheets (TiNS) synthesis in an optimized microwave-assisted flow reactor, followed by ion-exchange with a Pt precursor, before triggering the titanate layer rolling to trap the Pt precursor clusters inside the titania nanotubes, followed by a thermal treatment. TEM, XRD, and Raman analyses confirm the total conversion of TiO_2 into TiNS in 15 min at 120 °C and 4 bar, and the TiNS transformation into 181 nm-long TiNT with 10 and 6 nm outer and inner diameter, respectively. The 2% Pt-TiNT comprises 0.7 nm PtO clusters (according to XPS), causing slight distortions of the interlayer spaces, while a few larger 2–3 nm Pt clusters reside within the lumen. As a result, Pt-TiNT is 14-fold more active than TiNT for visible light (400–780 nm) photocatalytic oxidation of diclofenac under 2136 $\mu W \cdot cm^{-2}$ irradiation, and>1000-fold better than the uncatalyzed photoconversion reaction under 100 $mW \cdot cm^{-2}$ artificial solar lighting. In addition, nano-confinement of PtO clusters narrowed the bandgap of the TiNT, which, combined with its excellent absorptivity to harvest light, allowed a broader spectral range of photon energies to activate the photocatalyst.

1. Introduction

Titania nanotubes (TiNT) have potential applications in the environment, energy, and biomedicine, ranging from photocatalysts and sensors [1–3] to solar cells, batteries, and H_2 storage [4–6], as well as biomaterials for implants and drug delivery [7,8]. These 1D structures are wide band-gap semiconductors characterized by their large surface area, open porosity, versatile chemistry, and good stability [9,10]. The most popular preparation method is alkaline hydrothermal conversion [11,12], as it is simple, reliable, straightforward, and gives a high yield of nanotubular titania at moderate to low temperatures [13,14] with tailored crystallinity and surface area [15,16]. Although the debate on the mechanism is far from settled, it is recognized that lamellar titanates are a crucial intermediate in forming nanotubes.

The dissolution of TiO_2 creates TiNT during the NaOH hydrothermal treatment when the Ti-O-Ti bond is cleaved and converted to Ti-O-Na accompanied by epitaxial growth of layered nanosheets through an Ostwald ripening process, followed by the curving, and rolling of nanosheets into nanotubes [10]. The metallization of titania nanotubes is central to their applications in electrical circuitries, sensors, (photo)

* Corresponding author at: Department of Chemical and Environmental Engineering & Division of Environment and Sustainability, The Hong Kong University of Science and Technology, Clear Water Bay, Kowloon, Hong Kong Special Administrative Region.
** Co-corresponding author at: CSIC-ICP, Instituto de Catálisis y Petroleoquímica, Spectroscopy and Industrial Catalysis (SpeiCat), Marie Curie 2, E-28049-Madrid, Spain.
E-mail address: kekyeung@ust.hk (K.L. Yeung).

https://doi.org/10.1016/j.cej.2023.143254
Received 12 January 2023; Received in revised form 21 April 2023; Accepted 27 April 2023
Available online 2 May 2023

catalysis, and antibacterial material [17–20]. Incorporating Pt during the titanate nanosheets (TiNS) wrapping process allows their location within the lumen and interlayer spaces without resorting to complex preparation methods that include direct deposition of nanoparticles [21] and photo-deposition processes [21,22]. To date, Pt can only be incorporated within the nanotube lumen by a complex templating process using a sacrificial carbon nano coil [23] or by an ion exchange of metal cations into the nanotube structure followed by a reduction of the metal ion [24].

The conventional alkaline hydrothermal TiNT synthesis process is slow and energy-intensive, so the use of microwave (MW) rapid volumetric heating has been proposed as a green and economically competitive intensification process to speed up TiNT production and facilitate control over the reaction and product [25,26], as it promotes uniform crystallization, nanoparticle growth [27,28], Ostwald ripening [29], and solid–liquid interactions [30]. The MW flow reactors, first proposed in the 1990s, are designed to address the shortcomings of batch microwave reactors, including shallow penetration depth, inhomogeneities, and poor scalability [31]. It has gained significant popularity in recent years with the advancement in design and equipment, including the efficient monomode MW cavities [32]. Indeed, it has been explored for synthesis of various nanoparticles.

This work proposes an innovative synthesis method for the continuous and selective production of the TiNS. It exploits the unique geometry and formation mechanism of titania nanotubes to confine nanoparticles within the lumen and interlayer spaces of the material to endow TiNT with new properties. It has the further advantage of preventing particles from aggregating, leaching, and obstructing the nanotube pores. The intermediate TiNS are isolated in an optimized microwave-assisted flow reactor at a short residence time by rapid heating and quenching of the reaction in the monomode cavity. The PtO semi-metallic nanoparticles are then inserted into the TiNT's intraspaces to alter the bandgap structure of the semiconductor, facilitate electron transport, and promote charge separation.

The Pt-TiNT activity as a photocatalyst was investigated under UVA and visible light irradiation and compared to that of TiNT and a reference P25 TiO_2 photocatalyst [33], using diclofenac degradation as a case study. Diclofenac is a non-steroidal, anti-inflammatory drug popularly used as an analgesic [34,35] and is frequently found in the aquatic environment, as its removal in wastewater treatment plants varies from 7% to 98% [35–38]. Despite its low concentration, extended exposure could lead to chronic toxicological effects [39]. The photocatalytic oxidation of diclofenac can mitigate its anti-estrogenic properties and genotoxicity and, more importantly, prevent the generation of toxic transformation products [40]. Moreover, the visible light Pt-TiNT photocatalyst remained active following four repeated reaction cycles without regeneration.

2. Experimental

2.1. Materials

Anatase titanium dioxide (TiO_2, >99.8%, trace metal basis), sodium hydroxide pellets (NaOH, ≥98%), tetraammineplatinum(II) nitrate ($Pt(NH_3)_4.(NO_3)_2$, 99.995% trace metals basis), and ammonium nitrate (NH_4NO_3, ≥99.0%), and absolute ethanol were provided by Sigma-Aldrich (USA) and Merck KGaA (Germany), while nitric acid (HNO_3, 68%) and ammonium hydroxide (NH_4OH, 28%) were purchased from analaR NORMAPUR (Ecuador). Distilled deionized (DDI) water from Milli Q UF-Plus water purification system was used to synthesize and prepare Pt-TiNT. The photocatalytic oxidation (PCO) reaction was conducted on diclofenac sodium (DFS, ≥98.5%) from Sigma-Aldrich (USA). Trifluoroacetic acid (TFA, >99.0%) was supplied by Sigma-Aldrich (USA), while acetonitrile (CAN, >99.99%) was from RCI Labscan. *Photobacterium phosphoreum* (Nanjing Institute of Soil Science), *Salmonella typhimurium* NM2009 (IWAKI), and recombinant *Saccharomyces cerevisiae* (Xenometrix AG) were used for microtoxicity, SOS/umu genotoxicity, and yeast anti-estrogenic screen (YAS) bioactivity measurements with mercury (II) chloride (99.998%), 4-nitroquinoline 1-oxide (99.5%), 17 β-estradiol (≥98%), and Tamoxifen (≥98%) from Sigma-Aldrich (USA), as the corresponding calibration compounds.

2.2. TiNS microwave-assisted flow synthesis

A 1.9 g anatase TiO_2 was added to 250 ml of 10 M NaOH solution. The mixture was stirred for 1 h and ultrasonicated for 10 min to disperse TiO_2 into a stable suspension. The TiO_2 suspension was fed by a high-pressure pump (Gilson 307) with flow rates of 1.3–2.7 ml·min^{-1} to a PTFE tubular reactor (0.97 cm inner diameter, 1.1 cm outer diameter, 55 cm length) inside a prototype monomode microwave system (CEINNMAT KORA) equipped with a 900 W, 2.45 GHz magnetron, as shown in Fig. 1a and S1.

The Kora microwave applicator consisted of a vertical brass arm attached to two filter elbows made of aluminum. The reflective surface of the machined monobloc ensured uniform microwave propagation radially (i.e., transversal) and along the length (i.e., longitudinal) of the applicator, maximizing direct heating of the reactor. The shallow microwave penetration depth into the synthesis solution (i.e., 3 mm, cf. SI) was compensated for by radial mixing under a plug flow condition, ensuring rapid temperature homogenization (ca. 5 min) as shown in Fig. 1b-c. The PTFE flow reactor resided inside the cavity allowing direct microwave irradiation and heating as the reactant flows from the inlet at the bottom of the applicator arm and exits at the top. The reactor inlet and outlet ports are located at the open end of the filter elbows to avoid microwave leakage. A computer-controlled, closed-circuit unit tunes the microwave. The instrument's control CEINNMAT software is installed on a laptop computer and connected via a USB interface cable. A safety device is installed a meter above the unit to automatically turn off the main power when microwave leakage exceeds 1.5 mW·cm^{-2}. A K-type thermocouple inserted 5 cm above the microwave heating zone monitored the outlet temperature (i.e., 90–135 °C). At the same time, the reactor pressure (i.e., 2–4 barg) was measured and adjusted by a set of pressure gauges (Wika A-10) and a pressure regulator (MAE HS200) installed at the reactor outlet.

2.3. TiNT and Pt-TiNT preparation

The flow synthesis product, the raw titanate nanosheets, was converted to TiNT by centrifuging and washing with hot DDI water (80 °C) repeatedly until the pH equals 7, followed by drying in a vacuum oven at 60 °C for 12 h. Pt-TiNT was prepared by washing the raw titanate nanosheets with a platinum solution obtained by dissolving 0.78 g of $Pt(NH_3)_4.(NO_3)_2$ in 50 ml DDI before adding 50 g of NH_4NO_3. The solution was then cooled in an ice bath before adding 15 ml of 3 M ammonia solution slowly. Next, the pH was adjusted to 6 by adding a small amount of 1 M HNO_3. Finally, 100 ml absolute alcohol was added to give a 0.01 M $Pt(NH_3)_4.NO_3$ solution. Washing was performed until neutral pH, followed by centrifugation and vacuum drying at 60 °C for 12 h before air calcination at 300 °C for 3 h to obtain Pt-TiNT.

2.4. Material characterization

A Renishaw inVia™ micro-Raman spectroscopy system analyzed the TiNS, TiNT, and Pt-TiNT. The Raman microscope (RM 3000) is equipped with dual laser sources (Ar, 514.5 nm, 20 mW; He-Ne, 632.8 nm, 20 mW) and a 100 cm^{-1} cut-off notch filter. Raman spectra were collected under 50× magnification in the 100–1200 cm^{-1} window at a resolution of 1 cm^{-1}. Moreover, a Raman spectral mapping quantified the anatase TiO_2 conversion and titanate nanosheet yield from the microwave-assisted flow synthesis. A point-by-point raster mapping mode took measurements over a 15 × 15 μm^2 area at a step size of 2.5 μm.

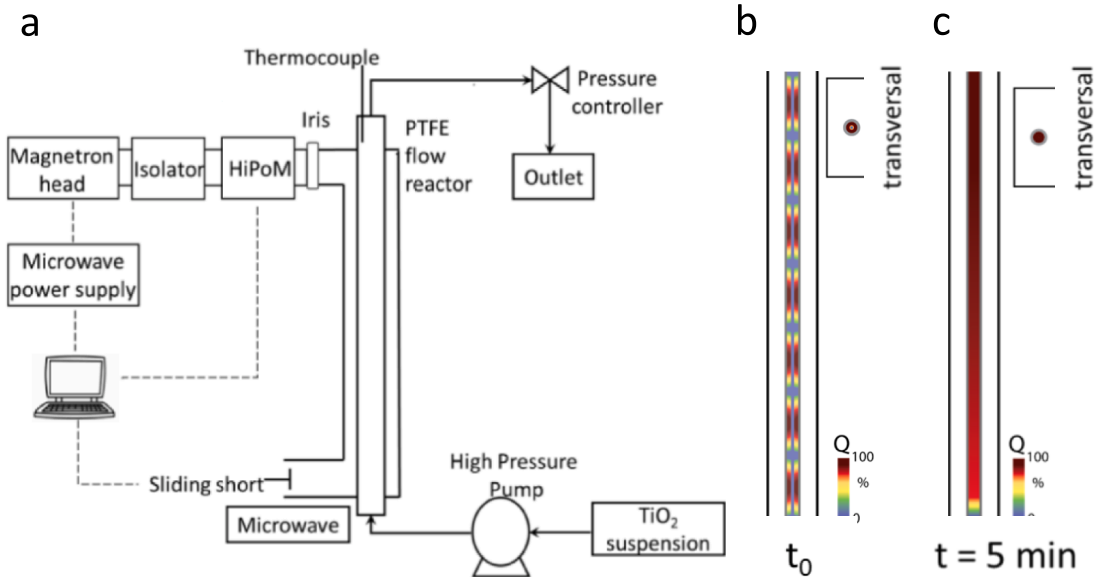

Fig. 1. A schematic diagram of (a) the microwave flow reactor and the calculated (b) initial (t_0) and (c) steady state ($t \geq 5$ min) thermal conversion of microwave radiation along the longitudinal and transversal (inset) sections of the reactor inside the Kora microwave applicator.

Powder X-ray diffraction was collected from 2θ of 5° to 80° with a step size of 0.0334° using a CuKα X-ray source and a Ni filter in a PANanalytical XPERT-PRO X-ray diffractometer. In addition, the samples were observed under a JEOL 2010 transmission electron microscope (TEM) equipped with an Oxford energy dispersive X-ray spectrometer with an Oxford silicon drift detector (SDD) and under a JEOL 2100F high-resolution TEM (i.e., 0.19 nm point resolution). The powder samples were dispersed in absolute ethanol under ultrasonication, and a drop was placed on a holey carbon-coated copper grid (400 mesh, TED Pella). Excess liquid was carefully removed with a filter paper wick and dried in a desiccator. The images were taken at accelerating voltages between 50 and 300 kV and a beam current of 100 pA·cm^{-2}. X-ray photoelectron and valence band spectra of TiNT and Pt-TiNT samples were obtained by Kratos Axis Ultra DLD multi-technique surface analysis system equipped with a dual (Al/Mg) and a monochromatic Al X-ray source. The spectra were referenced against C1s (284.8 eV) and analyzed by XPSPeak 4.1. In addition, diffuse reflectance spectra were collected by a Perkin Elmer Lambda 950 equipped with an integrating sphere to determine their bandgap using a tauc plot.

2.5. Diclofenac photocatalytic oxidation

Pt-TiNT, TiNT, Degussa P25 TiO_2, and Pt-P25 were tested for the degradation of diclofenac in a photocatalytic reactor under ultraviolet (UVA) and visible light irradiation. A 0.2 g catalyst sample was dispersed in 100 ml of 55 ppm diclofenac sodium solution and placed in a cylindrical quartz photoreactor (ID = 40 mm, h = 100 mm). The reaction was conducted in a metal enclosure equipped with either two Sankyo-Denki 6 W UVA lamps (F6T5BLB Blacklight Blue Lamp, 352 nm) providing an irradiance of 4524 μW·cm^{-2} or two GE 6 W white light lamps (F6T5 35 Fluorescent Lamp) equipped with a 400 nm cut-off filter and delivering 2136 μW·cm^{-2} to the photoreactor. Two direct currents (DC) fans recirculate the air in the reaction chamber and maintain the temperature at 24 ± 2 °C. Thermocouples monitored the air and reactor wall temperatures, while a stirrer ensured a well-mixed reaction. The experiment was conducted under 8 h of darkness and 24 h of UVA or visible light irradiation. Samples were taken at fixed time intervals, filtered through a Minisart 16532-K 0.22 μm syringe filter, and analyzed by Waters Acquity ultra-performance liquid chromatography (UPLC) equipped with an Acquity BEH C18 column. The mobile phase was 0.02% trifluoroacetic acid in acetonitrile with 0.02% TFA in water as a buffer. The flow rate of the mobile phase was 0.4 ml·min^{-1}.

The photolysis of diclofenac under sunlight was investigated for 100 ppm diclofenac dissolved in DDI water in a 150 ml stirred quartz reactor irradiated by an AM-1.5G sun simulator with an irradiance of 100 mW·cm^{-2}. Aliquots of the solution were collected and analyzed by AB SCEIX TripleTOFTM 4600 UPLC-MS/MS with an ACQUITY BEH C18 column. The mass spectra were obtained using positive electrospray ionization (ESI^+) between m/z 50 to m/z 1000 at a 100 Hz data acquisition rate. The MS/MS spectra was generated at 40 eV collision energy. The data acquisition and analysis were made by Analyst® 1.6.1 software and PeakView® 2.2 software. Aliquots were also tested for microtoxicity, genotoxicity, and anti-estrogenic activity. The luminescence of *Photobacterium phosphoreum* measured by Berthold LB 960 luminometer following 15 min exposure to an aliquot of the solution gives its microtoxicity as calibrated against $HgCl_2$ [41]. The genotoxicity was determined by an SOS/umu assay using *Salmonella typhimurium NM2009* and calibrated against 4-nitroquinoline 1-oxide (4NQO) [42]. The anti-estrogenic activity was assayed by a recombinant *Saccharomyces cerevisiae* yeast cells [43] by adding 17-β-estradiol (E2) with a concentration of 40 nM was added to each sample aliquot and its anti-estrogenic property measured against Tamoxifen.

3. Results and discussion

3.1. Characterization of the TiNS obtained by Microwave-Assisted flow synthesis

The microwave-assisted flow synthesis produces the intermediate TiNS that can be converted to TiNT after washing with water. At a residence time of 15 min and a reaction temperature of 120 °C under a reactor pressure of 4 barg, TiO_2 was completely converted into TiNS (Fig. 2a) with a narrow mean diameter of 55 ± 7 nm (Fig. 2b) and cannot be detected by XRD and Raman analysis (Fig. 2c, d). Fig. 2c presents the powder X-ray diffraction of the anatase TiO_2 reagent and the harvested TiNS after centrifugation and drying at 65 °C for 24 h. Anatase TiO_2 displays diffraction peaks consistent with JCPDS no. 21-1272, while TiNS domains seem too small to generate a diffraction pattern. Only the diffraction peaks of Na_2CO_3 (JCPDS no. 37-0451) are apparent, mainly present as contaminants from sodium hydroxide and a

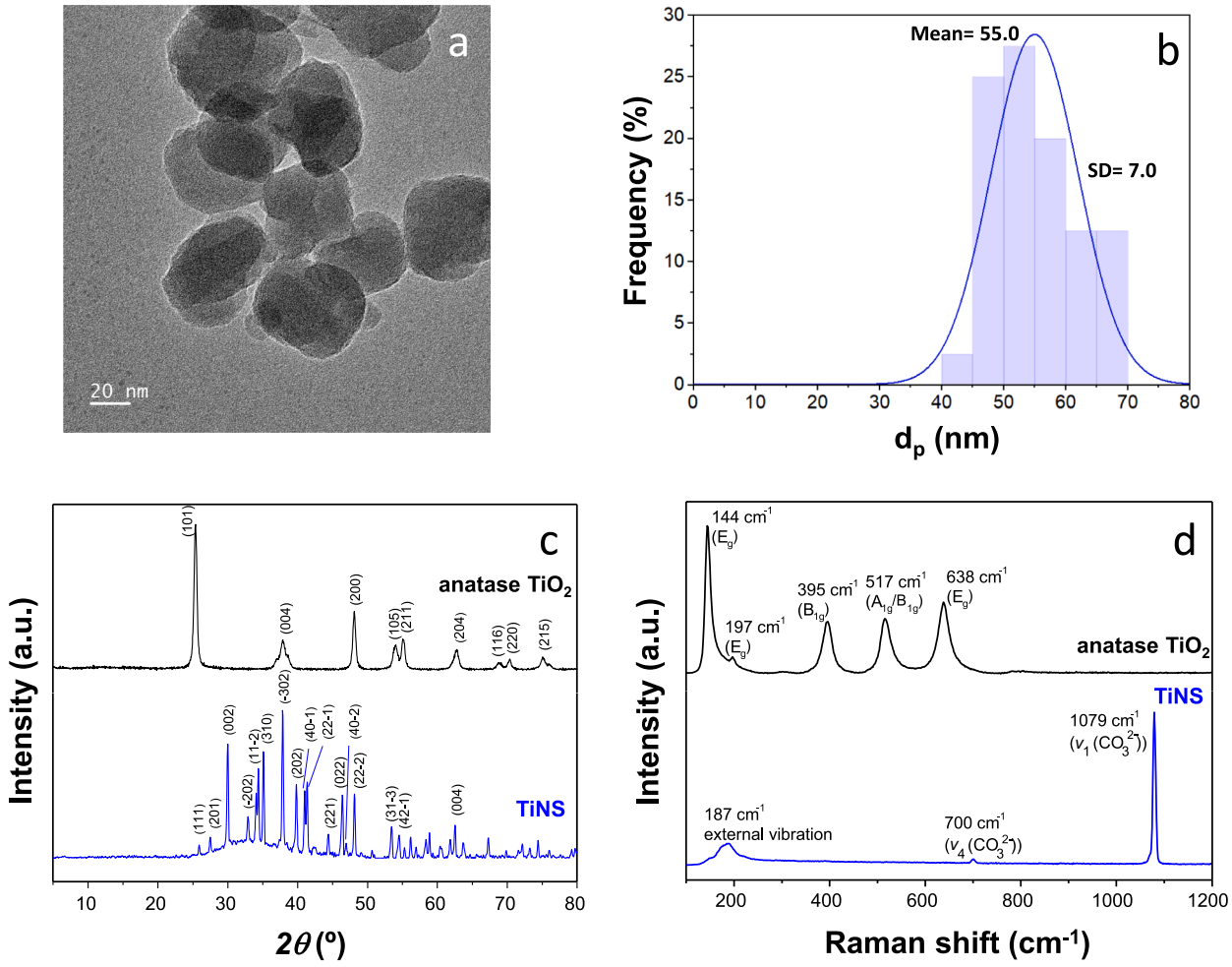

Fig. 2. (a) Transmission electron micrograph and (b) size distribution of TiNS produced by a microwave-assisted synthesis method and (c) the X-ray diffraction patterns and (d) Raman spectra of the precursor anatase TiO_2 and TiNS. Note: the synthesis condition is $[TiO_2] = 7.6$ g·L^{-1}, $[NaOH] = 10$ M, $\tau = 15$ min, T = 120 °C, and P = 4.0 barg.

by-product of the reaction of sodium hydroxide with dissolved carbon dioxide during the hydrothermal synthesis reaction.

Fig. 2d shows the corresponding micro-Raman spectra of the anatase TiO_2 reagent with its characteristic bands at 144 cm^{-1} (E_g), 197 cm^{-1} (E_g), 395 cm^{-1} (B_{1g}), 517 cm^{-1} (A_{1g}/B_{1g}), and 638 cm^{-1} (E_g), and the product of the synthesis. The intense band at 1079 cm^{-1} belongs to the ν_1 symmetric stretching vibration of CO_3^{2-} and the weaker band at 700 cm^{-1} arises from the ν_1 asymmetric bending mode of CO_3^{2-}. The 187 cm^{-1} band is attributed to external vibration between the cationic and anionic groups [44]. Therefore, the absence of TiNS Raman bands suggests a strong screening effect by the carbonate overlayer.

After washing the TiNS with hot DDI water followed by dewatering under centrifugation, titania nanotubes (Fig. 3a) were formed by progressive rolling of the titanate nanosheets, as proposed by Kasuga et al. [10], and unlike observations made by Wang et al. [45] that titania nanotube formation occurred during hydrothermal conversion and the washing step mainly removes the sodium ions. The transformation of Ti-O-Na to Ti-OH during washing removes the electrostatic repulsion allowing the nanosheets to fold and roll up. The TiNT are uniform and have an outer diameter of 9.6 ± 1.3 nm (Fig. 3b), an inner diameter of 5.5 ± 0.9 nm (Fig. 3c), and a length of 181 ± 22 nm (Fig. 3d), giving a length-to-width aspect ratio of about 20 and interlayer spacing of around 1 nm.

The rolling process will also result in concomitant changes in the Ti-O bond lengths, angles, and lattice vibration. X-ray diffraction of the nanotube sample displays seven diffraction peaks at 10.3, 24.5, 28.3, 33.8, 39.8, 48.2, and 62.7° (Fig. 3e). Several distinct structural models based on tetragonal anatase TiO_2, monoclinic $H_2Ti_3O_7$ and $H_2Ti_4O_9$, orthorhombic $H_2TiO_5{\cdot}H_2O$ and $H_{0.7}Ti_{1.825}\square_{0.175}O_4{\cdot}H_2O$ (□: vacancy) have been proposed for the nanotube crystal structure [45–49]. The diffraction of prepared TiNT (Fig. 3e) best matched the orthorhombic $H_{0.7}Ti_{1.825}\square_{0.175}O_4{\cdot}H_2O$ lepidocrocite titanate with edge-sharing TiO_6 octahedra layers [48] or a strained monoclinic $H_2Ti_3O_7$ [49]. The curvature and nanostructure causing a broadening of the diffraction peaks.

Fig. 3f displays the sample's micro-Raman spectrum showing the characteristic bands for TiNT at 194, 276, 386, 448, 666, 827, and 917 cm^{-1} [11,50]. These modes are associated with the orthorhombic structure assigned to Ti-O lattice vibrations within a 2D lepidocrocite-type TiO_6 octahedral host layer. Although anatase, rutile, and nanotubular titania have the same octahedral TiO_6 building blocks, the nature of their assembly is very different in the nanotubes. XRD shows that the TiO_6 octahedra arrangement in TiNT resembles that of bulky layered titanates, particularly that of orthorhombic $H_{0.7}Ti_{1.825}\square_{0.175}O_4{\cdot}H_2O$ containing vacancies [47]. The vibration near 276 cm^{-1} appears related to these vacancies and is consistent with the progressive titration of this mode with hydrogen peroxide [51]. Thus, the bands at 276, 448, and 666 cm^{-1} can be attributed to the three A_g symmetric modes of framework Ti–O–Ti in protonic lepidocrocite titanate ($H_{0.7}Ti_{1.825}\square_{0.175}O_4{\cdot}H_2O$), corresponding to Ti-O-Ti stretching in edge-shared TiO_6 [47,52].

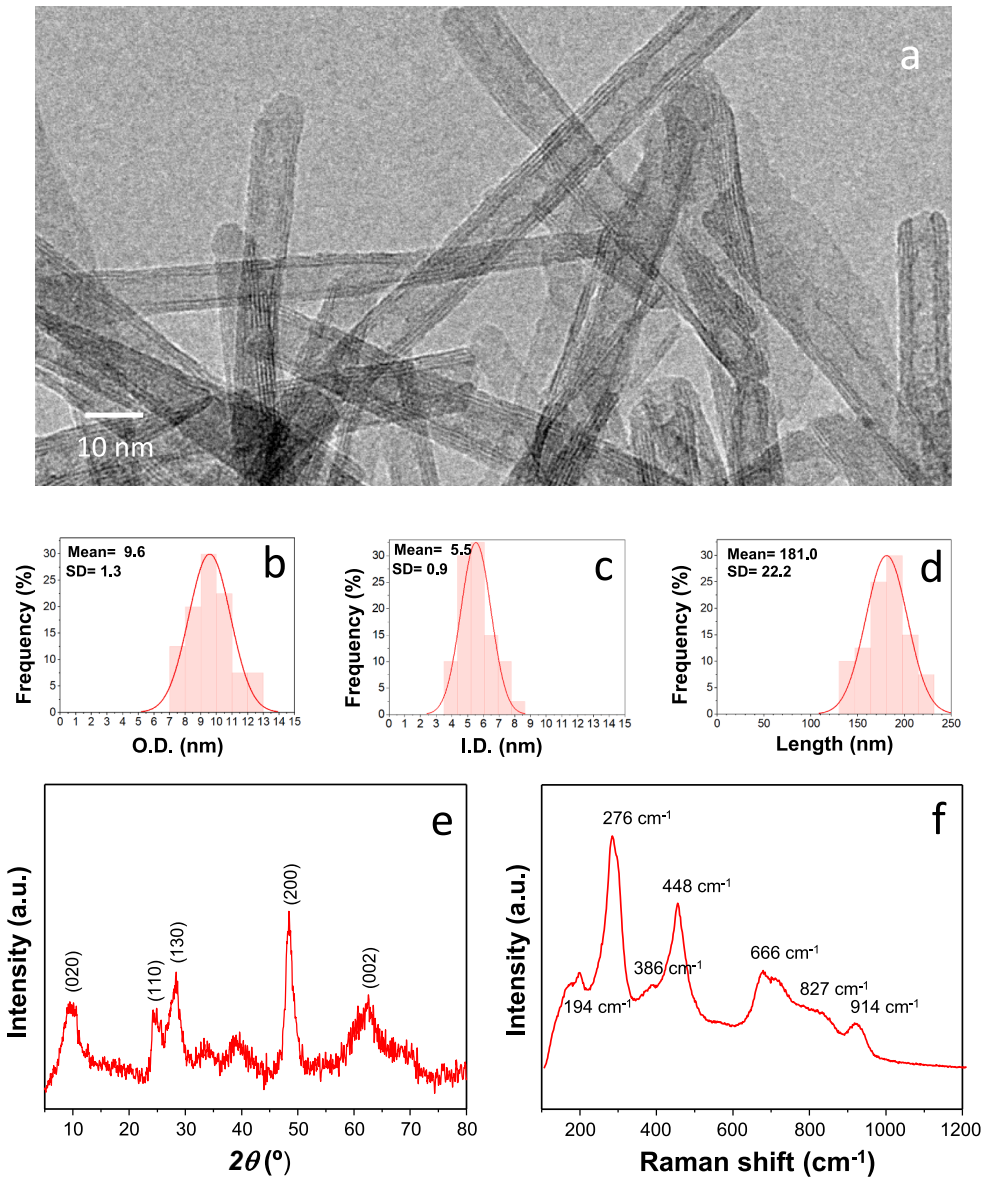

Fig. 3. (a) Transmission electron micrograph, and the size distributions of (b) outer diameter, (c) inner diameter, and (d) length of the TiNT and its corresponding (e) X-ray diffraction pattern and (f) Raman spectrum.

The bands in the 650–710 cm^{-1} region are characteristic of Ti-O vibrations in an octahedral environment; the frequency shift from bulky TiO_2 near 650 cm^{-1} to around 710 cm^{-1} in the nanotubes is attributed to a change in the long-range ordering of TiO_6 with the scrolling of the titanate layer. The Raman band at 827 cm^{-1} has been variously assigned to Ti-O on layer surface [53], a four-coordinated Ti-O vibration [10], and a short, symmetric Ti-O stretching mode [50]. It most likely belongs to the short Ti-O bond associated with non-bridging oxygen atoms coordinated to the interlayer cation [54,55]. The modes near 273 and 827 cm^{-1} are related to the covalent Ti-O-H bond found at the interlayers and, therefore, are also associated with the nanotube stability [56]. Finally, the vibration near 900 cm^{-1} could be related to Ti-O-H groups on the external surface [53].

3.2. Characterization of Pt-TiNT

Taking advantage of the formation mechanism of TiNT from TiNS, tetraamine platinum cations were ion-exchanged for the sodium of Ti-O-Na. The excess NH_4^+ in the ion-exchange solution suppressed TiNS from rolling, allowing the tetraamine platinum cations to disperse uniformly on the TiNS surface, and washing with hot acidified water triggered the rolling process, trapping the ion-exchanged platinum in the lumen and interlayer spaces to form Pt clusters (Fig. 4a) following heat treatment. Fig. 4a shows that with a Pt loading of 1.96 wt%, most Pt clusters are located within interlayer spaces and have a mean diameter of 0.7 ± 0.2 nm. It can be seen from the micrograph that insertion of Pt clusters causes localized distortion of the interlayer spacing, as the titanate layers deform to accommodate the clusters. The larger 2 to 3 nm Pt clusters reside mainly within the lumen (4.7 ± 0.8 nm). Fig. 4a inset presents a cross-sectional view of a Pt-TiNT showing a Pt cluster in the lumen and six clusters confined within the interlayers. A bright-field image of Pt-TiNT in Fig. 4b shows more clearly the Pt cluster size and locations in the nanotube. Each Pt-TiNT hosts approximately 300Pt clusters in its interlayer spaces, and roughly 25Pt clusters can be found within the lumen giving an estimated 2 wt% loading that is in good agreement with the experimental measurement. The layer distortions was also observed by XRD characterization since a broadening of the interlayer space was observed compared to the pristine TiNT (0.9 vs 0.8 nm).

The micro-Raman spectrum of freshly prepared Pt-TiNT in Fig. 4c

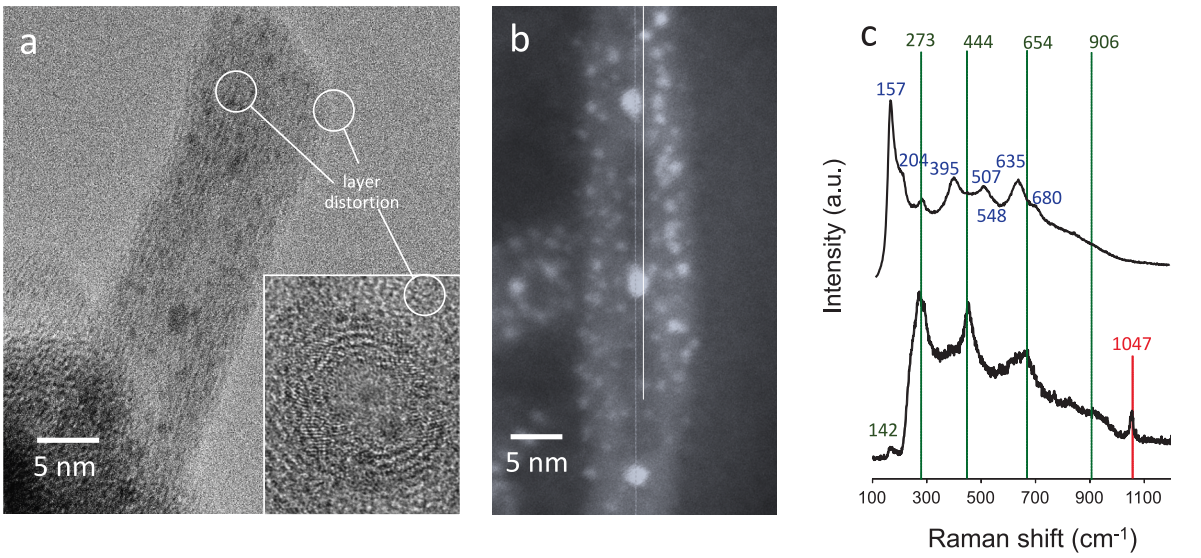

Fig. 4. (a) Dark field and (b) bright field transmission electron microscope images of Pt-TiNT with an inset micrograph of the nanotube cross-section in (a) and the corresponding (c) micro-Raman spectra of calcined Pt-TiNT (upper spectrum) and as prepared Pt-TiNT (lower spectrum).

displays the 273, 444, and 654 cm^{-1} bands of titania nanotube with a weak signal at 824 cm^{-1} from Ti-O coordinated to interlayer cation. The absence of the Ti-O-Na band at 917 cm^{-1} shows that the hot acid wash effectively removes sodium from the sample. Also present are the 1047 cm^{-1} band belonging to nitrate of the tetraamine platinum nitrate and a weak 142 cm^{-1} band attributed to distortion of the titanate layer from the ion-exchanged tetraamine platinum cations confined within the interlayer. The precursor decomposes, Pt clusters form during air calcination, and the nitrates were removed as indicated by the disappearance of 1047 cm^{-1} in the calcined Pt-TiNT.

Metal Pt is not Raman active, but PtO has Raman features at 438 cm^{-1} (E_g) and 657 cm^{-1} (B_{1g}), crystalline PtO_2 displays two sharp bands at 504 and 545 cm^{-1} ($A_{1g} + E_g$) while its amorphous form has a signal at 610 cm^{-1} [57,58]. The observed Raman signals at 507, 548 (shoulder), and 635 cm^{-1} suggest Pt is present as PtO_2 and PtO. The Raman bands at 273, 395, and 680 cm^{-1} are features of TiNT. The 444 cm^{-1} band is likely hidden within the overlapping PtO_x bands. The strong 157 cm^{-1} band with a shoulder at 204 cm^{-1} is interpreted to originate from the distorted 2D TiO_6 octahedral layers from inserted Pt clusters. Calcining protonic titanate at high temperature (ca. > 300 °C) can lead to the formation of monoclinic TiO_2(B) [59], but TEM evidence (Fig. 4a) suggests this is not the case for Pt-TiNT treated at 300 °C. N_2 physisorption measurement (Fig. S6 in SI) and helium pycnometer were conducted to determine their textural properties. Pt-TiNT displays a smaller BET surface area (213 ± 8 $m^2 \cdot g^{-1}$) and VSSA (60.4 ± 2.4 $m^2 \cdot cm^{-3}$) than TiNT (266 ± 30 $m^2 \cdot g^{-1}$ and 94.5 ± 10.0 $m^2 \cdot cm^{-3}$, respectively) as shown in Table 1. Similarly, it has smaller total and micropore volumes as the lumen and interlayer spaces are occupied by Pt clusters. The measured micropore diameter is bigger because of Pt clusters inserted between the titanate layers of Pt-TiNT.

Fig. 5 presents the X-ray photoelectron spectra for Pt 4f, Ti 2p, and O 1 s of Pt-TiNT after air calcination at 300 °C. Platinum is present primarily as PtO according to Fig. 5a, but minor contributions from PtO_2 cannot be excluded, particularly at the interface between the clusters and the titanate layers. The Ti 2p binding energies of 459.0 and 464.7 eV belonging Ti^{4+} (Fig. 5b) are lower compared to Ti 2p of TiNT of 458.6 and 464.3 eV. The increase in the Ti 2p binding energy suggests a decrease in the electron density around Ti atom and a possible indication of Pt-O-Ti bond formation [60]. The presence of a O 1 s peak at 535.2 eV in Fig. 5c could be attributed to foreshortening of the Ti-O bond due to PtO clusters confinement between titanate layers.

Fig. 6a presents the valence band spectra of TiNT and Pt-TiNT with energies of 3.00 and 2.95 eV, respectively. The reference photocatalyst, Degussa P25 TiO_2, has a reported valence band energy of 2.84–2.91 eV [61–63]. The bandgap energies are determined from the UV–Vis diffuse reflectance spectra (Fig. 6b) and the corresponding Tauc plot (Fig. S4 in SI). TiNT has a bandgap of 3.47 eV, while that of Pt-TiNT is 3.00 eV and the bandgap of Degussa P25 TiO_2 is reported to be 3.10–3.25 eV [63–65]. Together, this information gives the band edge positions of TiNT and Pt-TiNT as shown in Fig. 6c compared to the P25 TiO_2 benchmark.

According to the literature, PtO residing within the lumen and spaces between titanate layers, as in this study, are semi-metallic, exhibiting inverted conduction- and valence-band edges that are slightly overlapping [66]. Thus, PtO is electrically conducting, but its resistance displays a thermally activated transport. It also exhibits excellent optical absorption with increasing absorptivity with photon energy. XPS was unable to detect a measurable amount of PtO_2, and if present, PtO_2 will be mainly at the interface between PtO and titanate surface. Unlike PtO, PtO_2 displays a clear absorption edge and optical bandgap of 1.17 eV and has a much lower (100x smaller) optical absorption coefficient [67].

Table 1
TiNT and Pt-TiNT textural properties.

	TiNT	Pt-TiNT
BET surface area ($m^2 \cdot g^{-1}$)	266 ± 30	213 ± 8
VSSA ($m^2 \cdot cm^{-3}$)	94.5 ± 10.0	60.4 ± 2.4
Pore volume ($cm^3 \cdot g^{-1}$)	1.16 ± 0.03	0.96 ± 0.12
Micropore volume ($cm^3 \cdot g^{-1}$)	0.15 ± 0.02	0.08 ± 0.01
Micropore d_p (nm)	0.42 ± 0.12	0.65 ± 0.05

3.3. Natural photodegradation of diclofenac in water

Fig. 7a shows the simulated natural degradation of diclofenac in water under artificial sunlight. The 100-ppm diclofenac sodium photodegrades to form five major products (Fig. 7b). They are referred to according to their molecular mass as *m/z* 481, *m/z* 260, *m/z* 242, *m/z* 483, and *m/z* 495 in Fig. 7c. Exposure to sunlight causes the dimerization of diclofenac molecules to produce the bulky *m/z* 481 product containing two polar ethers. Photoreaction also causes the abstraction of a chlorine from diclofenac to form the product *m/z* 260, which is further transformed to product *m/z* 242 through hydrolysis with the substitution of hydroxyl for the sole remaining Cl atom. The hydroxylated *m/z* 242 product is expected to further oxidize to form quinone products

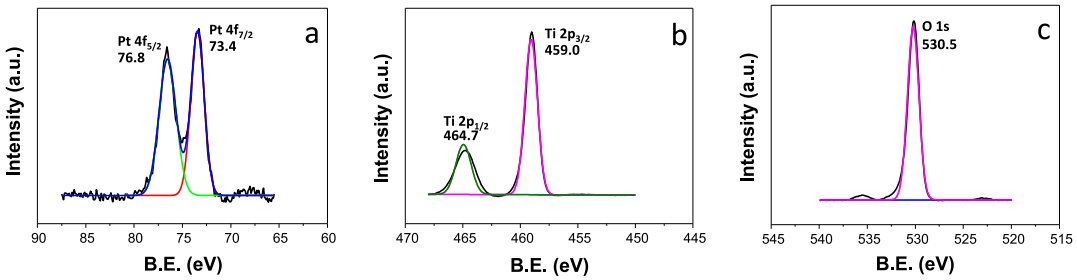

Fig. 5. X-ray photoelectron spectra of (a) Pt 4f, (b) Ti 2p, and (c) O 1s for Pt-TiNT.

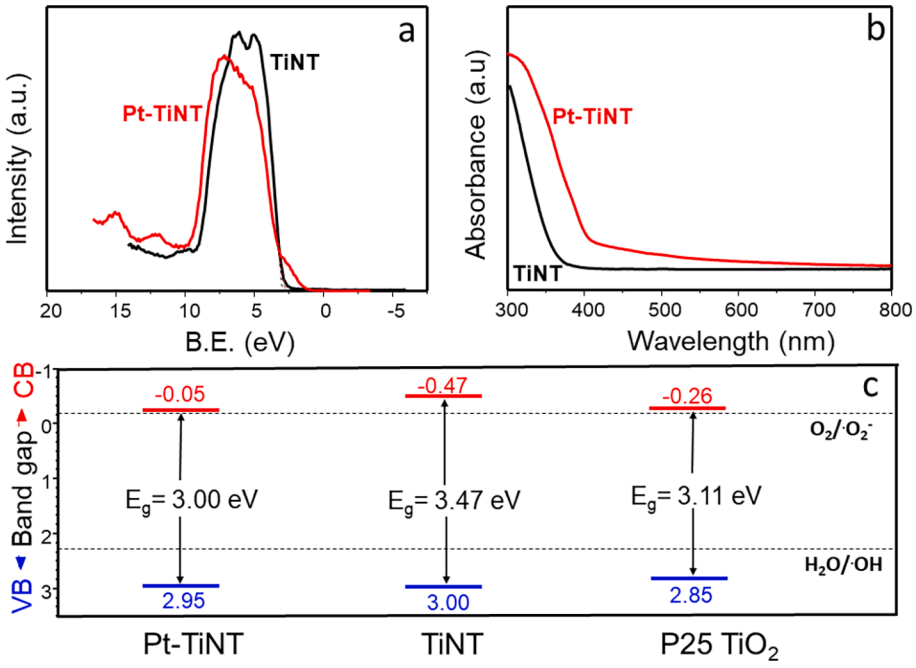

Fig. 6. (a) Valence-XPS and (b) diffuse reflectance UV–Vis spectra of TiNT and Pt-TiNT and (c) band edge positions of TiNT, Pt-TiNT, and P25 TiO_2.

[68,69] such as product *m/z* 256 that is found in trace amounts. The reactions of *m/z* 260 and *m/z* 242 with diclofenac produce monochlorinated *m/z* 483 and product *m/z* 495. Fig. 7b shows that the photodegradation of diclofenac leads to a corresponding increase in microtoxicity that correlates well with the formation of *m/z* 260 and *m/z* 483 chlorinated products.

According to SOS/umu assay in Fig. 8a, the genotoxicity decreases with diclofenac photodegradation, suggesting that it primarily arises from diclofenac rather than from its degradation products. The 100-ppm diclofenac is mildly genotoxic to Salmonella typhimurium, roughly equivalent to 3.49 ppm 4-NQO (i.e., an established carcinogenic and mutagenic compound). Prior work reports that even 20 ppm diclofenac is genotoxic to isogenic chicken DT40 mutant cell line [70]. In addition, diclofenac is a potent anti-estrogenic compound with an IC50 of 2.8 ppm. The measurements done by yeast anti-estrogenic screen assay require 25-fold dilutions to mitigate diclofenac's toxicity to the recombinant yeast. Even after dilution to 4 ppm, diclofenac still exerted a significant anti-estrogenic activity equivalent to 2.8 μM tamoxifen. Fig. 8b shows that the photodegraded diclofenac has lower anti-estrogenic properties. Still, a more efficient remediation process is needed to further mitigate its microtoxicity and anti-estrogenic properties.

3.4. Photocatalytic oxidation of diclofenac in water

A photocatalyst can accelerate diclofenac degradation in water and avoid the formation of toxic by-products, such as *m/z* 260 and *m/z* 483. For this purpose, TiNT and Pt-TiNT were tested as photocatalysts under UV and visible light for oxidations of diclofenac in water. Fig. 9 reports the PCO of diclofenac. Under black light illumination (4.5 $mW{\cdot}cm^{-2}$ UVA), P25 TiO_2 performed best (Fig. 9a), with a first-order rate constant (k) of 0.392 h^{-1}, followed by Pt-TiNT (k = 0.210 h^{-1}), with the unmodified TiNT being the least active (k = 0.091 h^{-1}). Using filtered visible lighting radiation (2.1 $mW{\cdot}cm^{-2}$), Pt-TiNT has the highest activity ($k = 0.268\ h^{-1}$) with Pt-P25 ($k = 0.015\ h^{-1}$), TiNT ($k = 0.021\ h^{-1}$) and P25 TiO_2 ($k = 0.045\ h^{-1}$) exhibiting poor activity (Fig. 9b). The PCO reaction did not generate any toxic by-products (i.e., *m/z* 260 and *m/z* 483). Indeed, only trace by-products were detected, indicating efficient mineralization of diclofenac (Fig. S5 of SI) in contrast to results of photoconversion under intense artificial sunlight (100 $mW{\cdot}cm^{-2}$) without photocatalyst (cf. Fig. 7). Table 2 lists the first-order rate constant and the apparent quantum efficiency (ϕ) for diclofenac conversion with and without photocatalysts under different light sources.

The ϕ-value for diclofenac photodegradation under artificial sunlight is negligible compared to the photocatalyzed reactions. Also, several of its transformation products were toxic and/or large and bulky. P25 TiO_2 photocatalyst's being a UV bandgap semiconductor performed poorly under visible light (ϕ = 1.8%), but the ϕ-value of 12.2% obtained under

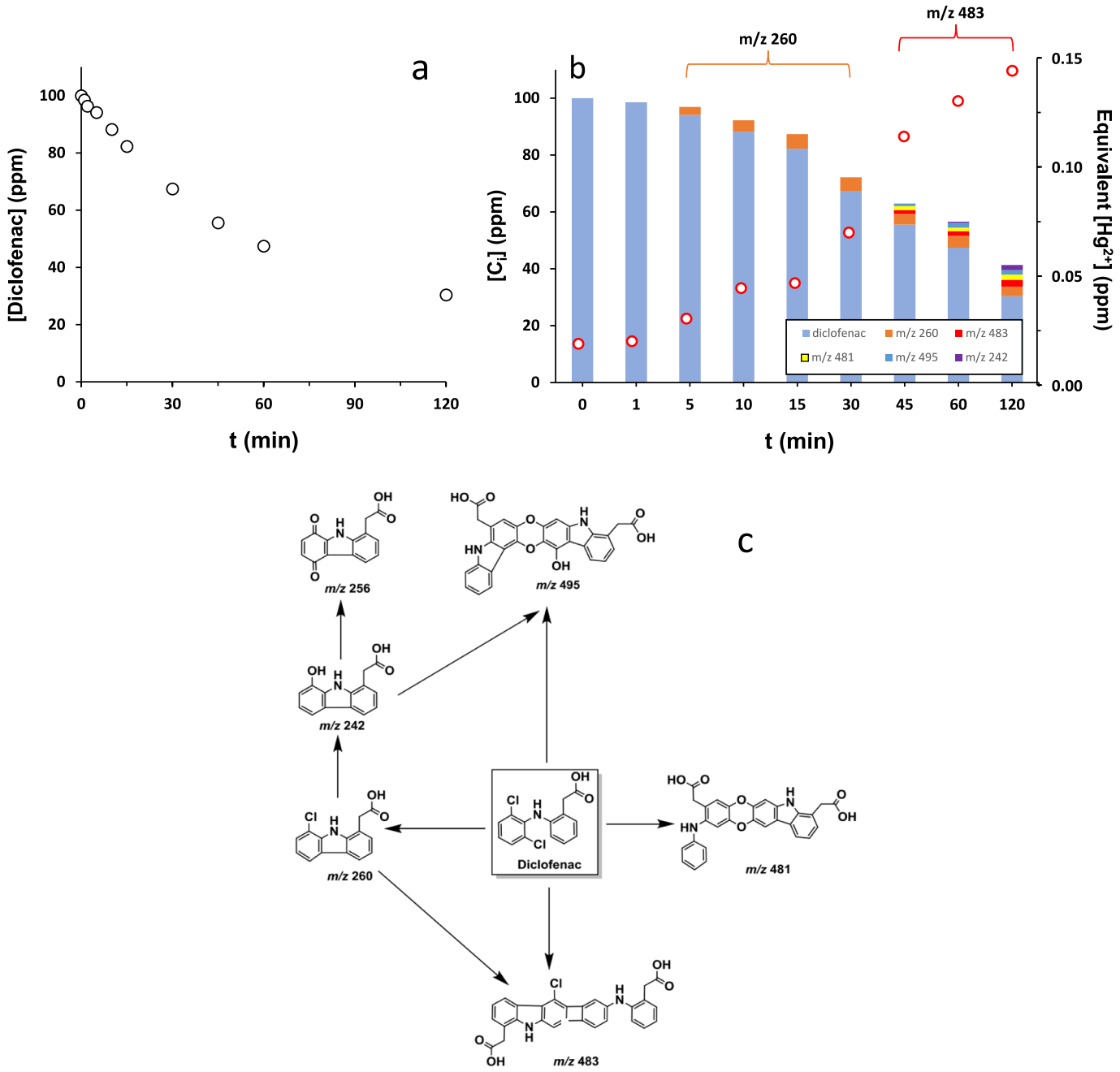

Fig. 7. Plots of (a) diclofenac concentration and (b) reaction composition (ppm) and microtoxicity (ppm Hg^{2+} equivalent) with irradiation time under artificial sunlight without photocatalyst (Note: left-axis in ppm concentration: blue bar, dichlofenac; orange bar, *m/z* 260 product; red bar, *m/z* 483 product; yellow bar, *m/z* 481 product; dark blue bar, *m/z* 495 product, and violet bar, *m/z* 242 product, right axis circles) and (c) proposed diclofenac transformation pathways. Note: $[diclofenac]_0 = 100$ ppm, $V_{batch} = 150$ ml, T = 27 ± 2 °C, 100 mW·cm^{-2} AM-1.5G sun simulator. (For interpretation of the references to colour in this figure legend, the reader is referred to the web version of this article.)

UV is comparable to values obtained for other pollutants, such as phenol (14%), chlorophenols (14–17%), and 2,4-dichlorophenol (14%) [67]. TiNT, having a larger bandgap, has poor activity under both UVA and visible light irradiation. Inserting PtO into TiNT's lumen and interlayer spaces narrows the bandgap. Moreover, PtO, like graphene, is a semi-metal and forms a Schottky barrier with the titanate layer promoting charge separation by trapping the electrons [62]. The fact that Pt-TiNT's conduction band edge is lower than P25 TiO_2 affects superoxide generation and could explain its lower reactivity under UVA. However, PtO's remarkable absorptivity enables it to efficiently harvest light and inject electrons into titania, thus boosting its performance under visible light by allowing a larger spectral range of photon energies to participate in photocatalysis. This process would be facilitated by PtO being highly dispersed within the interlayer spaces and in intimate contact with the titanate layers, as it would facilitate electron transport by allowing electrons to tunnel across the thin titanate layer. It could explain the 14-fold increase in ϕ compared to TiNT and more than a 1000-fold higher than uncatalyzed reaction (cf. Table 2).

4. Concluding remarks

This work illustrates a method for preparing confined nanoparticles

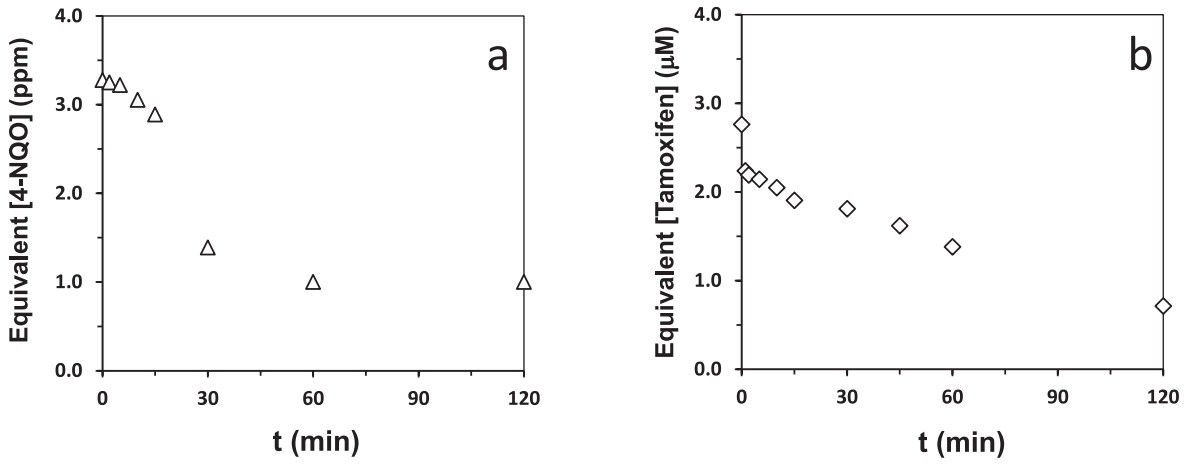

Fig. 8. Plots of (a) SOS/umu genotoxicity and (b) YAS anti-estrogenic activity of diclofenac over irradiation time under artificial sunlight and without photocatalyst. Note: $[diclofenac]_0 = 100$ ppm, $V_{batch} = 150$ ml, T = 27 ± 2 °C, 100 mW·cm^{-2} AM-1.5G sun simulator.

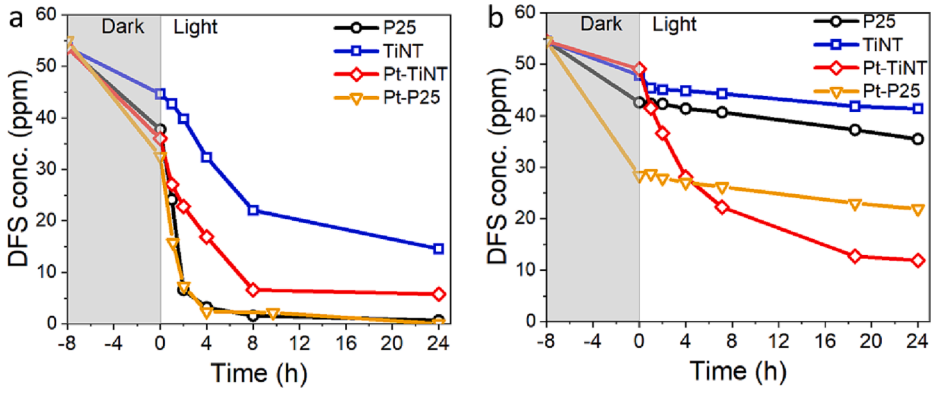

Fig. 9. Photocatalytic oxidation of diclofenac over Pt-TiNT, TiNT, Pt-P25 and P25 TiO_2 under (a) UVA and (b) visible light irradiation.

Table 2
Photodegradation of diclofenac.

	Light Source[1]					
	UVA		Visible Light		Artificial Sunlight	
	k (h^{-1})	ϕ (%)	k (h^{-1})	ϕ (%)	k (h^{-1})	ϕ (%)
No catalyst	–		–		0.886	*0.01*
P25	0.392	*12.2*	0.045	*1.8*	–	
TiNT	0.091	*2.8*	0.021	*0.8*	–	
Pt-P25	0.300	*9.3*	0.015	*0.6*	–	
Pt-TiNT	0.210	*6.6*	0.268	*11.2*	–	

[1] The apparent rate constant (k) was calculated from a first-order rate fitting of the experimental data and the apparent quantum efficiency (ϕ) was calculated from ratio of molecules of diclofenac converted and incident photon from the light source.

within the lumen and interlayer spaces of TiNT by manipulating its synthesis. First, TiNS were prepared and isolated by a microwave-assisted flow synthesis method, and the nanoparticles dispersed on its surface before initiating the rolling of the titanate layer, thus trapping the nanoparticles within its internal spaces. This approach was illustrated for Pt-TiNT, and the confinement of PtO clusters creates a photocatalyst active for photo-oxidation of diclofenac, a ubiquitous pharmaceutical pollutant of potent anti-estrogenic properties and mild genotoxicity. Pt-TiNT having a narrower bandgap than TiNT was active under visible and UVA lighting. The semi-metal PtO facilitated charge separation and electron transport. In addition, its excellent absorptivity let PtO act as an antenna for harvesting light, allowing the utilization of a broader spectral range of photon energies. The synthesis approach is applicable for the confinement of a broad range of clusters and nanoparticles, including metals, metal oxides, quantum dots, polymers, macromolecules, and compounds, to create new functionalities for TiNT. Future work will investigate the thermochemical processes during microwave-assisted titanium dioxide mineralization and transformation to TiNS. Furthermore, we will focus on the precise confinement of 0D, 1D, and 2D nanomaterials [71] within TiNT and investigate their properties and potential applications in catalysis [72]. Moreover, the metallization of TiNT will be explored [73].

Declaration of Competing Interest

The authors declare that they have no known competing financial interests or personal relationships that could have appeared to influence the work reported in this paper.

Data availability

Data will be made available on request.

Acknowledgements

This work is supported by the Horizon 2020 BIORIMA project and the Hong Kong Research Grant Council E-HKUST601/17 and in part by the Project of Hetao Shenzhen-Hong Kong University of Science and Technology Innovation Cooperation Zone (HZQB-KCZYB-2020083). Dr. Y.J. Luo stay at the Instituto de Catálisis y Petroleoquímica is supported

by the HKUST Overseas Research Award. Finally, the authors acknowledge the support of the Central Facilities of the Hong Kong University of Science and Technology including the Material Characterization and Preparation Facility (MCPF) and the Environmental Central Facility (ENVF).

Appendix A. Supplementary data

Supplementary data to this article can be found online at https://doi.org/10.1016/j.cej.2023.143254.

References

[1] N. Liu, X. Chen, J. Zhang, J.W. Schwank, A review on TiO_2-based nanotubes synthesized via hydrothermal method: formation mechanism, structure modification, and photocatalytic applications, Catal. Today 225 (2014) 34–51, https://doi.org/10.1016/j.cattod.2013.10.090.

[2] G. Wang, Q. Zhang, Q. Chen, X. Ma, Y. Xin, X. Zhu, D. Ma, C. Cui, J. Zhang, Z. Xiao, Photocatalytic degradation performance and mechanism of dibutyl phthalate by graphene/TiO_2 nanotube array photoelectrodes, Chem. Eng. J. 358 (2019) 1083–1090, https://doi.org/10.1016/j.cej.2018.10.039.

[3] D.V. Bavykin, F.C. Walsh, Elongated titanate nanostructures and their applications, Eur. J. Inorg. Chem. 8 (2009) 977–997, https://doi.org/10.1002/ejic.200801122.

[4] M. Madian, A. Eychmüller, L. Giebeler, Current advances in TiO_2-based nanostructure electrodes for high performance lithium ion batteries, Batteries 4 (2018) 7, https://doi.org/10.3390/batteries4010007.

[5] P. Roy, D. Kim, K. Lee, E. Spiecker, P. Schmuki, TiO_2 nanotubes and their application in dye-sensitized solar cells, Nanoscale 2 (2010) 45–59, https://doi.org/10.1039/B9NR00131J.

[6] R. Singh, S. Dutta, A review on H_2 production through photocatalytic reactions using TiO_2/TiO_2-assisted catalysts, Fuel 220 (2018) 607–620, https://doi.org/10.3390/batteries4010007.

[7] Y. Dong, X. Ji, A. Laaksonen, W. Cao, R. An, L. Lu, X. Lu, Determination of the small amount of proteins interacting with TiO_2 nanotubes by AFM-measurement, Biomaterials 192 (2019) 368–376, https://doi.org/10.1016/j.biomaterials.2018.11.013.

[8] Y. Huang, W. Wang, X. Zhang, X. Liu, Z. Xu, S. Han, Z. Su, H. Liu, Y. Gao, H. Yang, A prospective material for orthopedic applications: Ti substrates coated with a composite coating of a titania-nanotubes layer and a silver-manganese-doped hydroxyapatite layer, Ceram. Int. 44 (2018) 5528–5542, https://doi.org/10.1016/j.ceramint.2017.12.197.

[9] Á. Kukovecz, M. Hodos, E. Horváth, G. Radnóczi, Z. Kónya, I. Kiricsi, Oriented crystal growth model explains the formation of titania nanotubes, J. Phys. Chem. B 109 (2005) 17781–17783, https://doi.org/10.1021/jp054320m.

[10] D.V. Bavykin, V.N. Parmon, A.A. Lapkin, F.C. Walsh, The effect of hydrothermal conditions on the mesoporous structure of TiO_2 nanotubes, J. Mater. Chem. 14 (2004) 3370–3377, https://doi.org/10.1039/B406378C.

[11] T. Kasuga, M. Hiramatsu, A. Hoson, T. Sekino, K. Niihara, Formation of titanium oxide nanotube, Langmuir 14 (1998) 3160–3163, https://doi.org/10.1021/la9713816.

[12] D.V. Bavykin, F.C. Walsh, Titanate and Titania Nanotubes Synthesis: Properties and Applications, The Royal Society of Chemistry, Cambridge, UK, 2010.

[13] Y. Guo, N.-H. Lee, H.-J. Oh, C.-R. Yoon, K.-S. Park, W.-H. Lee, Y. Li, H.-G. Lee, K.-S. Lee, S.-J. Kim, Preparation of titanate nanotube thin film using hydrothermal method, Thin Solid Films 516 (2008) 8363–8371, https://doi.org/10.1016/j.tsf.2008.04.073.

[14] H. Ou, S. Lo, Review of titania nanotubes synthesized via the hydrothermal treatment: Fabrication, modification, and application, Sep. Purif. Technol. 58 (2007) 179–191, https://doi.org/10.1016/j.seppur.2007.07.017.

[15] C.L. Wong, Y.N. Tan, A.R. Mohamed, A review on the formation of titania nanotube photocatalysts by hydrothermal treatment, J. Environ. Manage. 92 (2011) 1669–1680, https://doi.org/10.1016/j.jenvman.2011.03.006.

[16] S. Sreekantan, C.w., Lai,, Study on the formation and photocatalytic activity of titanate nanotubes synthesized via hydrothermal method, J. Alloys Compd. 490 (2010) 436–442, https://doi.org/10.1016/j.jallcom.2009.10.030.

[17] W.T. Wahyuni, B.R. Putra, C. Harito, D.V. Bavykin, F.C. Walsh, T.D. James, G. Kociok-Kohn, F. Marken, Electroanalysis in 2D-TiO_2 nanosheet hosts: electrolyte and selectivity in ferroceneboronic acid-saccharide binding, Electroanalysis 30 (7) (2018) 1303–1310, https://doi.org/10.1002/elan.201700617.

[18] B. Riza Putra, C. Harito, D.V. Bavykin, F.C. Walsh, W. Tri Wahyuni, J.A. Boswell, A. M. Squires, J.M.F. Schmitt, M.A. Da Silva, K.J. Edler, P.J. Fletcher, A.E. Gesell, F. Marken, Processes associated with ionic current rectification at a 2D-titanate nanosheet deposit on a microhole poly (ethylene terephthalate) substrate, J. Solid State Electrochem. 23 (2019) 1237–1248, https://doi.org/10.1007/s10008-019-04199-4.

[19] L. Long, Y.u. Xiang, W.u. Liangpeng, J. Li, X. Li, Nano-CdS confined within titanate nanotubes for efficient photocatalytic hydrogen production under visible light illumination, Nanotechnology 25 (3) (2013), 035603, https://doi.org/10.1088/0957-4484/25/3/035603.

[20] D.A. Sales, T.M.F. Marques, A. Ghosh, S.B.S. Gusmão, T.L. Vasconcelos, C. Luz-Lima, O.P. Ferreira, L.M. Hollanda, I.S. Lima, E.C. Silva-Filho, D. Dittz, A.O. Lobo, B.C. Viana, Sales,, Synthesis of silver-cerium titanate nanotubes and their surface properties and antibacterial applications, Mater. Sci. Eng. C Mater. Biol. Appl. 115 (2020), 111051, https://doi.org/10.1016/j.msec.2020.111051.

[21] J.M. Macak, P.J. Barczuk, H. Tsuchiya, M.Z. Nowakowska, A. Ghicov, M. Chojak, S. Bauer, S. Virtanen, P.J. Kulesza, P. Schmuki, Self-organized nanotubular TiO_2 matrix as support for dispersed Pt/Ru nanoparticles: enhancement of the electrocatalytic oxidation of methanol, Electrochem. Commun. 7 (2005) 1417–1422, https://doi.org/10.1016/j.elecom.2005.09.031.

[22] Y.-Y. Song, Z.-D. Gao, P. Schmuki, Highly uniform Pt nanoparticle decoration on TiO_2 nanotube arrays: a refreshable platform for methanol electrooxidation, Electrochem. Commun. 13 (2011) 290–293, https://doi.org/10.1016/j.elecom.2011.01.006.

[23] J. Zhang, W. Yu, D. Feng, H. Xu, Y. Qin, Porous titania nanotube confined ultrafine platinum catalysts synthesized by atomic layer deposition with enhanced hydrolytic dehydrogenation performance, Appl. Catal. B Environ. 312 (2022), 121405, https://doi.org/10.1016/j.apcatb.2022.121405.

[24] F.C. Walsh, D.V. Bavykin, L. Torrente-Murciano, A.A. Lapkin, B.A. Cressey, Synthesis of novel composite materials via the deposition of precious metals onto protonated titanate (TiO_2) nanotubes, Trans. IMF 84 (2006) 293–299, https://doi.org/10.1179/174591906X149077.

[25] X. Wu, Q.-Z. Jiang, Z.-F. Ma, M. Fu, W.-F. Shangguan, Synthesis of titania nanotubes by microwave irradiation, Solid State Commun. 136 (2005) 513–517, https://doi.org/10.1016/j.ssc.2005.09.023.

[26] S.H. Cho, H.H. Nguyen, G. Gyawali, J.-E. Son, T. Sekino, B. Joshi, S.H. Kim, Y. H. Jo, T.H. Kim, S.W. Lee, Effect of microwave-assisted hydrothermal process parameters on formation of different TiO_2 nanostructures, Catal. Today 266 (2016) 46–52, https://doi.org/10.1016/j.cattod.2015.10.001.

[27] C.-H. Huang, Y.-T. Yang, R.-A. Doong, Microwave-assisted hydrothermal synthesis of mesoporous anatase TiO_2 via sol–gel process for dye-sensitized solar cells, Microporous and Mesoporous Mater. 142 (2011) 473–480, https://doi.org/10.1016/j.micromeso.2010.12.038.

[28] A. Kumar, Y. Kuang, Z. Liang, X. Sun, Microwave chemistry, recent advancements, and eco-friendly microwave-assisted synthesis of nanoarchitectures and their applications: a review, Mater. Today Nano 11 (2020), 100076, https://doi.org/10.1016/j.mtnano.2020.100076.

[29] P.E.J. Saloga, C. Kästner, A.F. Thünemann, High-speed but not magic: microwave-assisted synthesis of ultra-small silver nanoparticles, Langmuir 34 (2018) 147–153, https://doi.org/10.1021/acs.langmuir.7b01541.

[30] F.B. Simoes, L.M. Da Silva, T.O. Fonseca, L.E. Almeida, E.A. dos Santos, Isolated effects of microwave radiation on the solid-liquid interface reactions between hydroxyapatite nanocrystals and silver ions, Ceram. Int. 44 (2018) 16960–16971, https://doi.org/10.1016/j.ceramint.2018.06.137.

[31] L. Estel, M. Poux, N. Benamara, I. Polaert, Continuous flow-microwave reactor: where are we? Chem. Eng. Process. 113 (2017) 56–64, https://doi.org/10.1016/j.cep.2016.09.022.

[32] Q. Saleem, M. Torabfam, T. Fidan, H. Kurt, M. Yuce, N. Clarke, M.K. Bayazit, Microwave-promoted continuous flow systems in nanoparticle synthesis-a perspective, ACS Sustainable Chem. Eng. 9 (2021) 9988–10015, https://doi.org/10.1021/acssuschemeng.1c02695.

[33] F. Fresno, R. Portela, S. Suárez, J.M. Coronado, Photocatalytic materials: recent achievements and near future trends, J. Mater. Chem. A. 2 (2014) 2863–2884, https://doi.org/10.1039/C3TA13793G.

[34] R.N. Brogden, R.C. Heel, G.E. Pakes, T.M. Speight, G.S. Avery, Diclofenac sodium: a review of its pharmacological properties and therapeutic use in rheumatic diseases and pain of varying origin, Drugs 20 (1980) 24–48, https://doi.org/10.2165/00003495-198020010-00002.

[35] P. Sathishkumar, R.A.A. Meena, T. Palanisami, V. Ashokkumar, T. Palvannan, F. L. Gu, Occurrence, interactive effects and ecological risk of diclofenac in environmental compartments and biota – A review, Sci. Total Environ. 698 (2020), 134057, https://doi.org/10.1016/j.scitotenv.2019.134057.

[36] M. Rosset, L.W. Sfreddo, G.E.N. Hidalgo, O.W. Perez-Lopez, L.A. Féris, Adsorbents derived from hydrotalcites for the removal of diclofenac in wastewater, Appl. Clay Sci. 175 (2019) 150–158, https://doi.org/10.1016/j.clay.2019.04.014.

[37] I. Alessandretti, C.V.T. Rigueto, M.T. Nazari, M. Rosseto, A. Dettmer, Removal of diclofenac from wastewater: a comprehensive review of detection, characteristics and tertiary treatment techniques, J. Environ. Chem. Eng. 9 (6) (2021), https://doi.org/10.1016/j.jece.2021.106743.

[38] N. Vieno, M. Sillanpää, Fate of diclofenac in municipal wastewater treatment plant — A review, Environ. Int. 69 (2014) 28–39, https://doi.org/10.1016/j.envint.2014.03.021.

[39] L. Lonappan, S.K. Brar, R.K. Das, M. Verma, R.Y. Surampalli, Diclofenac and its transformation products: environmental occurrence and toxicity – A review, Environ. Int. 96 (2016) 127–138, https://doi.org/10.1016/j.envint.2016.09.014.

[40] K. Fischer, S. Sydow, J. Griebel, S. Naumov, C. Elsner, I. Thomas, A.A. Latif, A. Schulze, Enhanced removal and toxicity decline of diclofenac by combining UVA treatment and adsorption of photoproducts to polyvinylidene difluoride, Polymers 12 (10) (2020) 2340, https://doi.org/10.3390/polym12102340.

[41] L.P. Li, J.K.C. Kwan, K.L. Yeung, An investigation of the transformation, kinetics and bioactivity of ozone treatment of DEET in water, Chem. Eng. J. 368 (2019) 10–17, https://doi.org/10.1016/j.cej.2019.02.157.

[42] Y. Oda, S. Nakamura, I. Oki, T. Kato, H. Shinagawa, Evaluation of the new system (umu-test) for the detection of environmental mutagens and carcinogens, Mutat. Res., Genet. Toxicol. Environ. Mutagen. 147 (1985) 219–229, https://doi.org/10.1016/0165-1161(85)90062-7.

[43] E.J. Routledge, J.P. Sumpter, Estrogenic activity of surfactants and some of their degradation products assessed using a recombinant yeast screen, Environ. Toxicol. Chem. 15 (1996) 241–248, https://doi.org/10.1002/etc.5620150303.

[44] N. Buzgar, A.I. Apopei, The Raman study of certain carbonates, Geologie. Tomul LV 2 (2009) 97–112.
[45] Y.Q. Wang, G.Q. Hu, X.F. Duan, H.L. Sun, Q.K. Xue, Microstructure and formation mechanism of titanium dioxide nanotubes, Chem. Phys. Lett. 365 (2002) 427–431, https://doi.org/10.1016/S0009-2614(02)01502-6.
[46] R. Ma, Y. Bando, T. Sasaki, Nanotubes of lepidocrocite titanates, Chem. Phys. Lett. 380 (2003) 577–582, https://doi.org/10.1016/j.cplett.2003.09.069.
[47] T. Gao, H. Fjellvåg, P. Norby, Crystal structures of titanate nanotubes: a Raman scattering study, Inorg. Chem. 48 (2009) 1423–1432, https://doi.org/10.1021/ic801508k.
[48] T. Sasaki, M. Watanabe, Y. Michiue, Y.u. Komatsu, F. Izumi, S. Takenouchi, Preparation and acid-base properties of a protonated titanate with the lepidocrocite-like layer structure, Chem. Mater. 7 (5) (1995) 1001–1007.
[49] O.P. Ferreira, A.G. Souza, J.M. Filho, O.L.A. Filhob, Unveiling the structure and composition of titanium oxide nanotubes through ion exchange chemical reactions and thermal decomposition processes, J. Braz. Chem. Soc. 17 (2006) 393–402.
[50] M.A. Cortés-Jácome, G. Ferrat-Torres, L.F.F. Ortiz, C. Angeles-Chávez, E. López-Salinas, J. Escobar, M.L. Mosqueira, J.A. Toledo-Antonio, In situ thermo-Raman study of titanium oxide nanotubes, Catal. Today 126 (2007) 248–255, https://doi.org/10.1016/j.cattod.2007.02.012.
[51] M.A. Khan, H.-T. Jung, O.-B. Yang, Opto-electronic properties of titania nanotubes, Chem. Phys. Lett. 458 (2008) 134–137, https://doi.org/10.1016/j.cplett.2008.04.073.
[52] B.C. Viana, O.P. Ferreira, A.G.S. Filho, A.A. Hidalgo, J.M. Filho, O.L. Alves, Alkali metal intercalated titanate nanotubes: a vibrational spectroscopy study, Vib. Spectrosc. 55 (2011) 183–187, https://doi.org/10.1016/j.vibspec.2010.11.007.
[53] T. Gao, H. Fjellvåg, P. Norby, Raman Scattering Properties of a Protonic Titanate $H_xTi_{2-x/4\ x/4}O_4{\cdot}H_2O$ (, vacancy; x= 0.7) with Lepidocrocite-Type Layered Structure, J. Phys. Chem. B 112 112 (31) (2008) 9400–9405.
[54] C.E. Bamberger, G.M. Begun, Sodium titanates: stoichiometry and Raman spectra, J. Am. Ceram. Soc. 70 (3) (1987) C-48–C-51.
[55] M. Shirpour, J. Cabana, M. Doeff, Lepidocrocite-type layered titanate structures: new lithium and sodium ion intercalation anode materials, Chem. Mater. 26 (2014) 2502–2512, https://doi.org/10.1021/cm500342m.
[56] L. Qian, Z.-L. Du, S.-Y. Yang, Z.-S. Jin, Raman study of titania nanotube by soft chemical process, J. Mol. Struct. 749 (2005) 103–107, https://doi.org/10.1016/j.molstruc.2005.04.002.
[57] J.R. McBride, G.W. Graham, C.R. Peters, W.H. Weber, Growth and characterization of reactively sputtered thin-film platinum oxides, J. Appl. Phys. 69 (1991) 1596–1604, https://doi.org/10.1063/1.347255.
[58] W. Lin, A.A. Herzing, C.J. Kiely, I.E. Wachs, Probing metal− support interactions under oxidizing and reducing conditions: in situ Raman and infrared spectroscopic and scanning transmission electron microscopic− X-ray energy-dispersive spectroscopic investigation of supported platinum catalysts, J. Phys. Chem. C 112 (2008) 5942–5951, https://doi.org/10.1021/jp710591m.
[59] K.K. Paul, R. Ghosh, P.K. Giri, Mechanism of strong visible light photocatalysis by Ag_2O-nanoparticle-decorated monoclinic TiO_2(B) porous nanorods, Nanotechnology 27 (31) (2016), https://doi.org/10.1088/0957-4484/27/31/315703.
[60] M.C. Biesinger, L.W. Lau, A.R. Gerson, R.S. Smart, Resolving surface chemical states in XPS analysis of first row transition metals, oxides and hydroxides: Sc, Ti, V, Cu and Zn, Appl. Surf. Sci. 257 (2010) 887–898, https://doi.org/10.1016/j.apsusc.2010.07.086.
[61] Y. Fang, Y. Huang, Z. Ni, Z. Wang, S. Kang, Y. Wang, X. Li, Co-modified commercial P25 TiO_2 by Fe doping and g-C_3N_4 coating as high performance photocatalyst under visible light irradiation, Int. J. Electrochem. Sci. 12 (2017) 5951–5963, https://doi.org/10.20964/2017.07.77.
[62] Y. Xu, Y. Luo, Q. Qian, B. Huang, Q. Chen, Simple fabrication of BiOCl/Bi/P25 composite with enhanced visible light photocatalytic activity, Opt. Mater. 72 (2017) 691–696, https://doi.org/10.1016/j.optmat.2017.07.027.
[63] S. Taghavi, A. Amoozadeh, F. Nemati, The first report of deep eutectic solvent (DES) nano-photocatalyst (n-TiO_2-P25@TDI@DES (urea: $ZnCl_2$)) and its application on selective oxidation of benzyl alcohols to benzaldehydes, J. Chem. Technol. Biotechnol. 96 (2021) 384–393, https://doi.org/10.1002/jctb.6550.
[64] X. Chen, C. Burda, The electronic origin of the visible-light absorption properties of C-, N- and S-doped TiO_2 nanomaterials, J. Am. Chem. Soc. 130 (2008) 5018–5019, https://doi.org/10.1021/ja711023z.
[65] L.-L. Tan, W.-J. Ong, S.-P. Chai, A.R. Mohamed, Band gap engineered, oxygen-rich TiO_2 for visible light induced photocatalytic reduction of CO_2, Chem. Commun. 50 (2014) 6923–6926, https://doi.org/10.1039/C4CC01304B.
[66] H. Neff, S. Henkel, E. Hartmannsgruber, E. Steinbeiss, W. Michalke, K. Steenbeck, H.G. Schmidt, Structural, optical, and electronic properties of magnetron-sputtered platinum oxide films, J. Appl. Phys 79 (1996) 7672–7675, https://doi.org/10.1063/1.362341.
[67] N. Serpone, A. Salinaro, Terminology, relative photonic efficiencies and quantum yields in heterogeneous photocatalysis. Part I: suggested protocol, Pure Appl. Chem. 71 (1999) 303–320, https://doi.org/10.1351/pac199971020303.
[68] T.J. Monks, R.P. Hanzlik, G.M. Cohen, D. Ross, D.G. Graham, Quinone chemistry and toxicity, Toxicol. Appl. Pharmacol. 112 (1992) 2–16, https://doi.org/10.1016/0041-008X(92)90273-U.
[69] L. Zhang, Y. Liu, Y. Fu, Degradation kinetics and mechanism of diclofenac by UV/peracetic acid, RSC Adv. 10 (2020) 9907–9916, https://doi.org/10.1039/D0RA00363H.
[70] X. Liu, J. Lee, K. Ji, S. Takeda, K. Choi, Potentials and mechanisms of genotoxicity of six pharmaceuticals frequently detected in freshwater environment, Toxicol. Lett. 211 (2012) 70–76, https://doi.org/10.1016/j.toxlet.2012.03.003.
[71] K.Y. Ho, K.L. Yeung, Properties of TiO_2 support and the performance of Au/TiO_2 catalyst for CO oxidation reaction, Gold Bull. 40 (2007) 15–30, https://doi.org/10.1007/BF03215288.
[72] K.L. Yeung, W.K. Leung, N. Yao, S.L. Cao, Reactivity and antimicrobial properties of nanostructured titanium dioxide, Catal. Today 143 (2009) 218–224, https://doi.org/10.1016/j.cattod. 2008.09.036.
[73] K.L. Yeung, J.M. Sebastian, A. Varma, Novel preparation of Pd/Vycor composite membranes, Vatal. Today 25 (1995) 231–236, https://doi.org/10.1016/0920-5861(95)00077-S.